Intercomparison of Mesoscale Model Simulations of the Daytime Valley Wind System

JUERG SCHMIDLI,[a] BRIAN BILLINGS,[b] FOTINI K. CHOW,[c] STEPHAN F. J. DE WEKKER,[d] JAMES DOYLE,[e] VANDA GRUBIŠIĆ,[f] TEDDY HOLT,[e] QIANGFANG JIANG,[e] KATHERINE A. LUNDQUIST,[c] PETER SHERIDAN,[g] SIMON VOSPER,[g] C. DAVID WHITEMAN,[h] ANDRZEJ A. WYSZOGRODZKI,[i] AND GÜNTHER ZÄNGL[j]

[a] *National Center for Atmospheric Research, Boulder, Colorado, and Institute for Atmospheric and Climate Science, ETH, Zurich, Switzerland*
[b] *Desert Research Institute, Reno, Nevada, and Naval Research Laboratory, Monterey, California*
[c] *University of California, Berkeley, Berkeley, California*
[d] *Department of Environmental Sciences, University of Virginia, Charlottesville, Virginia*
[e] *Naval Research Laboratory, Monterey, California*
[f] *Desert Research Institute, Reno, Nevada, and Department of Meteorology and Geophysics, University of Vienna, Vienna, Austria*
[g] *Met Office, Exeter, United Kingdom*
[h] *Department of Atmospheric Sciences, University of Utah, Salt Lake City, Utah*
[i] *National Center for Atmospheric Research, Boulder, Colorado*
[j] *Deutscher Wetterdienst, Offenbach, Germany*

(Manuscript received 27 May 2010, in final form 19 October 2010)

ABSTRACT

Three-dimensional simulations of the daytime thermally induced valley wind system for an idealized valley–plain configuration, obtained from nine nonhydrostatic mesoscale models, are compared with special emphasis on the evolution of the along-valley wind. The models use the same initial and lateral boundary conditions, and standard parameterizations for turbulence, radiation, and land surface processes. The evolution of the mean along-valley wind (averaged over the valley cross section) is similar for all models, except for a time shift between individual models of up to 2 h and slight differences in the speed of the evolution. The analysis suggests that these differences are primarily due to differences in the simulated surface energy balance such as the dependence of the sensible heat flux on surface wind speed. Additional sensitivity experiments indicate that the evolution of the mean along-valley flow is largely independent of the choice of the dynamical core and of the turbulence parameterization scheme. The latter does, however, have a significant influence on the vertical structure of the boundary layer and of the along-valley wind. Thus, this ideal case may be useful for testing and evaluation of mesoscale numerical models with respect to land surface–atmosphere interactions and turbulence parameterizations.

1. Introduction

Over mountain areas the evolution of the boundary layer is particularly complex as a result of the interaction between boundary layer turbulence and thermally induced mesoscale wind systems, such as the slope and valley winds (e.g., Rotach et al. 2008). As the horizontal resolution of operational forecasts progresses to finer resolution, a larger spectrum of thermally induced wind systems can be explicitly resolved. It is therefore useful to document the current state-of-the-art of mesoscale models in simulating the coupled evolution of the mountain boundary layer and the valley wind system.

The mean structure of the slope and valley winds has been well investigated and is described in numerous reviews (e.g., Wagner 1938; Egger 1990; Whiteman 1990, 2000). Slope winds are understood to arise as a consequence of horizontal density gradients between the surface layer over the slopes and the air over the center of the valley. The

Corresponding author address: Juerg Schmidli, Institute for Atmospheric and Climate Science, ETH Zurich, Universitätsstrasse 16, 8092 Zurich, Switzerland.
E-mail: jschmidli@env.ethz.ch

DOI: 10.1175/2010MWR3523.1

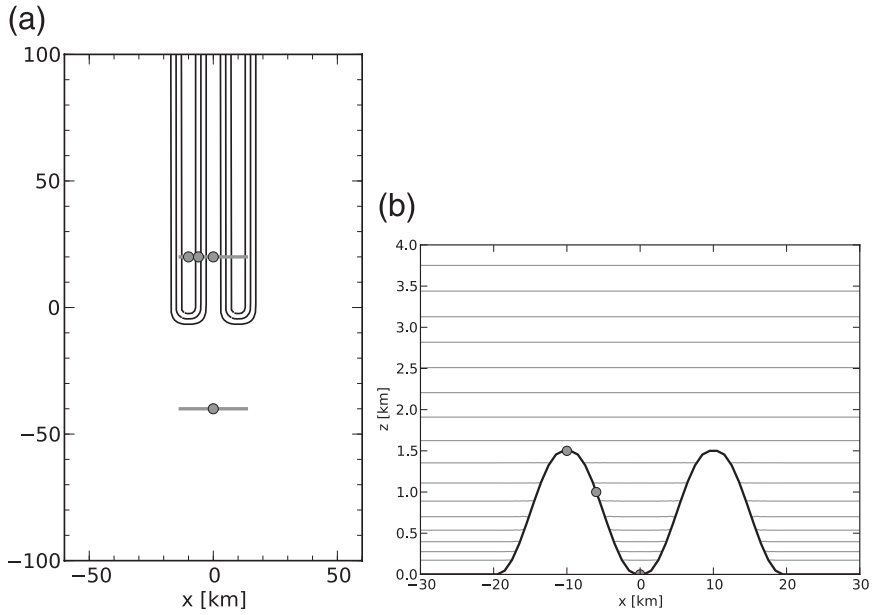

FIG. 1. (a) Contour plot of the three-dimensional valley-plain topography (contour values are 250, 750, and 1250 m) and computational domain adopted; only the southern half of the domain is shown. The gray lines denote the locations of the vertical cross sections and the circles denote the locations of the soundings to be shown. (b) Cross section of topography and initial potential temperature distribution (contour interval is 1 K).

diurnal along-valley winds are generated by locally developed along-valley pressure gradients. These pressure gradients are produced hydrostatically from temperature differences that form along the valley axis. The origin of these temperature differences is often explained by the topographic amplification factor (TAF) concept (Wagner 1938; Steinacker 1984; McKee and O'Neil 1989). The interaction between the thermally induced flows and turbulent processes over complex terrain has been investigated in recent field campaigns and modeling studies, such as the Mesocale Alpine Programme (MAP; e.g., Rotach et al. 2004; Weigel et al. 2007) and the Vertical Transport and Mixing campaign (VTMX; e.g., Doran et al. 2002; Zhong and Fast 2003). While these and other modeling studies showed that mesoscale models can skillfully simulate important aspects of the mountain boundary layer, they also pointed to the sensitivity of the results to physical parameterizations and to substantial differences among the models in the strength of the simulated terrain-induced circulations (e.g., Zhong and Fast 2003; Chow et al. 2006).

In this paper we present an intercomparison of valley wind simulations for an idealized valley–plain configuration using 9 mesoscale models with a grid spacing of 1 km. The aim of the paper is to document the valley wind system simulated by the nine models and to explore (i) the significance of varying the dynamical core, (ii) the uncertainties associated with the parameterization of subgrid-scale mixing and turbulence, and (iii) the uncertainties associated with the parameterization of radiation transfer and surface–atmosphere interactions. Thus apart from an idealized topography, the setup of the simulations is as close as possible to real-case simulations. The models are run with comprehensive model physics including a radiation transfer scheme, land surface scheme, and turbulence parameterization. A large computational domain and periodic lateral boundary conditions are used in order to eliminate lateral boundary effects, which were found to significantly influence simulation results in previous model intercomparison studies (Doyle et al. 2000; Thunis et al. 2003). This intercomparison project was conducted as part of the Terrain-Induced Rotor Experiment (T-REX), which took place in Owens Valley, California, in March–April 2006 (Grubisic et al. 2008). The field campaign was complemented by several modeling efforts.

2. Experimental design

a. Setup

The intercomparison is based on the idealized valley–plain system shown in Fig. 1. This setup is similar to configurations used in previous studies (Li and Atkinson 1999; Rampanelli et al. 2004; Schmidli and Rotunno 2010). The topography was chosen to satisfy the criteria listed in Rampanelli et al. (2004): 1) A horizontal valley

TABLE 1. Model formulation for dynamics and mixing. The finite difference algorithms are referred to as centered in time (CIT), forward in time (FIT), off-centered in time (OIT), leapfrog (LF), Runge–Kutta (RK), centered in space (CIS), upstream in space (UIS), split-explicit (SE), semi-implicit (SI), and semi-Lagrangian (SL). The turbulence parameterizations used for the convective boundary layer (CBL) are referred to as penetrative convection scheme (PCS), "nonlocal K" approach (NLK), Deardorff-based TKE closure (D-TKE), and Mellor–Yamada-based TKE closure (MY-TKE). Further abbreviations include: h for horizontal, v for vertical, NL for nonlocal turbulent length scale, LOC for local turbulent length scale, c for computational mixing, iso for isotropic, and BSIC for model base state equals the initial condition profile.

Model	Time diff	Δt (s)	Advection	Turbulence parameter for CBL (vertical mixing)	Horizontal mixing	BSIC
ARPS v5.2.8	SE-CIT Second-order LF	12	Fourth-order CIS (v: Second order)	1.5-order D-TKE, NL (Sun and Chang 1986)	c: Fourth order, 0.001 s^{-1}	Yes
COSMO v4.10.1	SE-FIT Third-order RK	12	Fifth-order UIS (v: Third order)	1.5-order MY-TKE, NL (Doms et al. 2007)	c: Fourth order, 0.001 s^{-1}	No
COAMPSv3 —	SE-CIT Second-order LF	3	Second-order CIS	1.5-order MY-TKE, NL (Thompson and Burk 1991)	c: Fourth order, 0.001 s^{-1}	Yes
COAMPSv4 v4.0	SE-CIT Second-order LF	3	Second-order CIS	1.5-order MY-TKE, NL (Thompson and Burk 1991)	c: Fourth order, 0.001 s^{-1}	Yes
EULAG —	FIT MPDATA	3	Second-order CIS	1.5-order D-TKE, LOC (Schumann 1991)	Second-order TKE iso	No
MM5 v3.6.1	SE-CIT Second-order LF	3	Second-order CIS	First-order PCS (Zhang and Anthes 1982)	c: Fourth order, 0.001 s^{-1} *	No
RAMS v6.0	SE-CIT Second-order LF	6	Second-order CIS	1.5-order MY-TKE, NL (Helfand and Labraga 1988)	Second-order Smagorinsky	Yes
UM v7.4	SI-OIT SI-SL	10	SI-SL	First-order NLK (Lock et al. 2000)	c: Fourth order, 0.001 s^{-1}	Yes
WRF-TKE v2.2	SE-FIT Third-order RK	1	Fifth-order UIS (v: Third order)	1.5-order D-TKE, LOC	Second-order TKE iso	Yes
WRF-YSU v2.2	SE-FIT Third-order RK	1	Fifth-order UIS (v: Third order)	First-order NLK (Hong et al. 2006)	Second-order Smagorinsky	Yes

* The z diffusion (Zängl 2002).

floor, so that the along-valley wind has no upslope contribution, 2) a long valley, so that the along-valley flow can develop unhindered from numerical boundary conditions in the along-valley direction, and 3) moderately steep valley slopes that can be adequately represented by current mesoscale models (the average slope is 9.6°). In contrast to previous studies, a large computational domain and periodic lateral boundary conditions were chosen to minimize the influence of the lateral boundaries on the simulated flow.

The analytical expression for the topography used is given by

$$z = h(x, y) = h_p h_x(x) h_y(y), \tag{1}$$

where

$$h_x(x) = \begin{cases} 0 & |x| \le X_1 \\ \frac{1}{2} - \frac{1}{2}\cos\left(\pi \frac{|x| - X_1}{S_x}\right) & X_1 < |x| < X_2 \\ 1 & X_2 \le |x| \le X_3 \\ \frac{1}{2} + \frac{1}{2}\cos\left(\pi \frac{|x| - X_3}{S_x}\right) & X_3 < |x| < X_4 \\ 0 & |x| \ge X_4 \end{cases} \tag{2}$$

and

$$h_y(y) = \begin{cases} 1 & |y| \le L_y \\ \frac{1}{2} + \frac{1}{2}\cos\left(\pi \frac{|y| - L_y}{S_y}\right) & L_y < |y| < L_y + S_y \\ 0 & |y| \ge L_y + S_y, \end{cases} \tag{3}$$

with valley depth $h_p = 1.5$ km, valley half-length $L_y = 100$ km, sloping sidewall width $S_x = S_y = 9$ km, $X_1 = 0.5$ km, $X_2 = 9.5$ km, $X_3 = 10.5$ km, $X_4 = 19.5$ km, and $X_3 - X_2 = 1$ km is the plateau width in the cross-valley direction. Even though the valley floor is quite narrow, the slopes are well represented at 1-km grid resolution.

The simulations are started from an atmosphere at rest. The initial condition for the atmosphere is given by the potential temperature distribution:

$$\theta(z) = \theta_s + \Gamma z + \Delta\theta[1 - \exp(-\beta z)], \tag{4}$$

where $\theta_s = 280$ K, $\Gamma = 3.2$ K km^{-1}, $\Delta\theta = 5$ K, and $\beta = 0.002$ m^{-1}, the surface pressure $p_s = 1000$ hPa, and a constant relative humidity of 40% is prescribed. The initial temperature profile describes an atmosphere with a constant stratification of $N \approx 0.011$ s^{-1} with a superimposed near-surface stable layer.

TABLE 2. Model formulation for the radiation transfer, soil temperature and soil–surface–atmosphere coupling. The characteristics of the radiation schemes are referred to as empirical methods (empirical), two-stream methods (two stream), and slope-dependent incoming solar radiation (SDR). The generation of the land surface scheme according to the classification of Sellers et al. (1997) is listed in the column LSM. Some characteristics of the soil–surface–atmosphere coupling are listed under the corresponding column including the temperature used in the surface energy budget (T_{sfc}), the resistances considered in calculating the total resistance (r_{sfc}) to the heat transfer between the surface (T_{sfc}) and the lowest model level, and the minimum total wind speed used for the calculation of the surface fluxes (u_{min}). Further abbreviations refer to solar radiation (SW), longwave radiation (LW), Rapid Radiative Transfer Model (RRTM; Mlawer et al. 1997), the Dudhia shortwave model (Dudhia; Dudhia 1989), thickness of the soil layers d, soil temperature T_{so}, canopy temperature T_c, skin temperature T_{sk}, friction velocity u_*, standard resistance based on Monin–Obukhov similarity theory r_a, and additional resistance to heat transfer r_d (e.g., roughness sublayer and laminar sublayer).

Model	Radiation	SDR	LSM	Soil temperature parameter	Soil–surface–atmosphere coupling
ARPS	Two stream (4 SW and 8 LW bands)	Yes	2	Force-restore (2 layers) d = 10 and 100 cm	$T_{sfc} = T_{so}$; $r_{sfc} = r_d + r_a$ u_{min} = 1 m s^{-1}
COSMO	Two stream (3 SW and 5 LW bands)	No	2	Eight-layer thermal diff d = 1, 2, 6, 18 cm, etc.	$T_{sfc} = T_{so}$; $r_{sfc} = r_d + r_a$ u_{min} = 0.01 m s^{-1}
COAMPSv3	Two stream (3 SW and 5 LW bands)	No	1	Force-restore (1 layer)	$T_{sfc} = T_{so}$; $r_{sfc} = r_d + r_a$ u_{min} = 1.0 m s^{-1}
COAMPSv4	Two stream (3 SW and 5 LW bands)	No	2	Four-layer thermal diff d = 10, 30, 60, 100 cm	$T_{sfc} = T_{sk}$; $r_{sfc} = r_d + r_a$ u_{min} = 0.1 m s^{-1}
EULAG	Empirical	Yes	1	Force-restore (1 layer) d = 11 cm	$T_{sfc} = T_{so}$; $r_{sfc} = r_a$
MM5	Two stream (RRTM LW, Dudhia SW)	Yes	1	Five-layer thermal diff d = 1, 2, 4, 8, 16 cm	$T_{sfc} = T_{so}$; $r_{sfc} = r_a$ $u_* \geq$ 0.1 m s^{-1}
RAMS	Two stream (Chen and Cotton 1983)	Yes	2	11-layer thermal diff d = 1, 3, 6, 9 cm, etc.	$T_{sfc} = T_{so}$, T_c; $r_{sfc} = r_d + r_a$
UM	Two stream (6 SW and 8 LW bands)	No	3	Four-layer thermal diff d = 10, 25, 65, 200 cm	$T_{sfc} = T_{sk}$; $r_{sfc} = r_d + r_a$ u_{min} = 0.001 m s^{-1}
WRF-TKE	Two stream (RRTM LW, Dudhia SW)	No	2	Four-layer thermal diff d = 10, 30, 60, 100 cm	$T_{sfc} = T_{sk}$; $r_{sfc} = r_d + r_a$
WRF-YSU	Two stream (RRTM LW, Dudhia SW)	No	2	Four-layer thermal diff d = 10, 30, 60, 100 cm	$T_{sfc} = T_{sk}$; $r_{sfc} = r_d + r_a$

The computational domain of the simulations is 400 km in the along-valley direction y and 120 km in the cross-valley direction x. The grid spacing is 1 km in both directions. In the vertical, the computational domain extends to 12.2 km and the grid spacing varies from 20 m near the ground to a maximum of 200 m above 2 km. The transition between the minimum and maximum vertical grid spacing was given by

$$\Delta z_i = \Delta z_m + \frac{\Delta z_{\min} - \Delta z_m}{\tanh 2\alpha} \tanh\left[\frac{2\alpha}{1-\alpha}(i-a)\right], \quad i = 1, \ldots, n,$$

where Δz_{min} = 20 m, Δz_m = 110 m, $a = (1 + n)/2$, α = 0.5, and n = 20. The lateral boundary conditions are periodic. A Rayleigh sponge layer, starting at 5 km, was specified as the top boundary condition. All simulations were run with the Coriolis force turned off.

The models were integrated for 12 h from sunrise at 0600 local time (LT) to sunset at 1800 LT. The temporal evolution of surface sensible heat flux is determined by the model physics; that is by the coupled land surface–atmosphere system. The incoming radiation is determined by the geographic location of the model domain which was set to 36°N, 0°, and the time of year which was set to 21 March 2007. Uniform land surface characteristics were used, which include a sandy loam soil, a semi-desert vegetation with a leaf area index (LAI) of 1.5, a vegetation fraction of 0.1, and a surface roughness length of 0.1 m. The surface albedo is determined implicitly in most models by the specified land surface characteristics. For the models where this is not the case, the albedo is set to 0.27. The soil temperature was initialized with the temperature of the lowest atmospheric level and the soil moisture saturation ratio was set to 20%, with the exception of the fifth-generation Pennsylvania State University–National Center for Atmospheric Research (PSU–NCAR) Mesoscale Model (MM5) for which the moisture availability was set to 20% (the MM5 soil model used does not include prognostic soil moisture; the latent heat flux is determined by multiplying potential evaporation with the moisture availability). It should be noted that the low initial value of atmospheric moisture and the very dry soil precluded the formation of any clouds (except for some radiatively insignificant clouds in MM5).

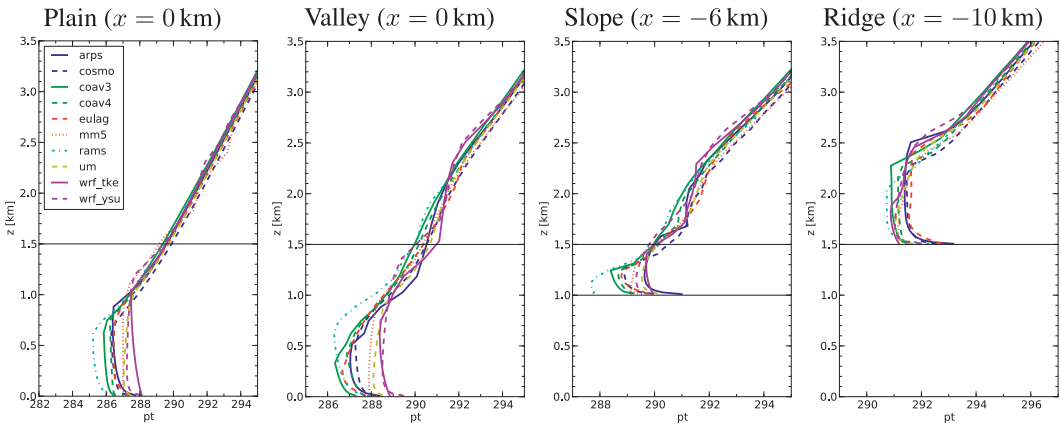

FIG. 2. Profiles of potential temperature (pt) at 1200 LT at (left to right) 4 different locations ($y = -40$ km for the plain, $y = 20$ km for the other three sites). The horizontal line at 1.5 km indicates the height of the mountain ridge.

b. *Models*

The following models were used in the intercomparison study: the Advanced Regional Prediction System (ARPS; Xue et al. 2000, 2001), the Consortium for Small-scale Modeling model (COSMO; Steppeler et al. 2003), the Coupled Ocean–Atmosphere Mesoscale Prediction System version 3 (COAMPSv3; Hodur 1997) and version 4 (COAMPSv4; Hodur 1997; Holt et al. 2006), the Eulerian–semi-Lagrangian model (EULAG; Prusa et al. 2008), MM5 (Dudhia 1993), the Regional Atmospheric Modeling System (RAMS; Cotton et al. 2003), the Met Office Unified Model (UM; Davies et al. 2005), and the Weather Research and Forecasting model (WRF; Skamarock and Klemp 2008). All of the models are nonhydrostatic with one making use of the anelastic equation set (EULAG), and the others solving the fully compressible equations. The vertical coordinates are terrain following. Significant differences among the models exist in the type of schemes used for the dynamics and physics. A brief description of some main characteristics of the models is given in Tables 1 and 2.

Turbulence in the convective boundary layer is represented by nonlocal first-order closure techniques in several models, either based on a mass flux approach (convective plume model; Estoque 1968; Blackadar 1978; MM5) or the *K*-profile method [Troen and Mahrt 1986; UM and WRF-Yonsei University (YSU)]. In contrast, an explicit predictive equation for turbulent kinetic energy (TKE) is employed by the other models. One group of models (COSMO, COAMPS, and RAMS) uses a standard *nonlocal* TKE closures based on Mellor–Yamada (Mellor and Yamada 1982), a second group (EULAG and WRF-TKE) uses

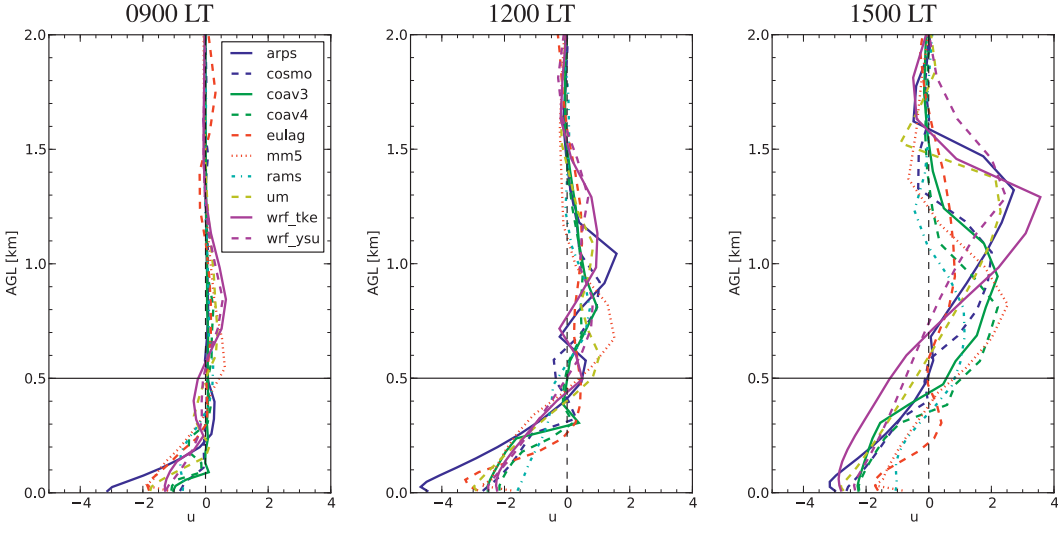

FIG. 3. Profiles of cross-valley wind speed u over the western slope ($x = -6$ km, $y = 20$ km) at (left to right) 0900, 1200, and 1500 LT. The y axis denotes the height above ground level, and the horizontal line indicates the height of the mountain ridge.

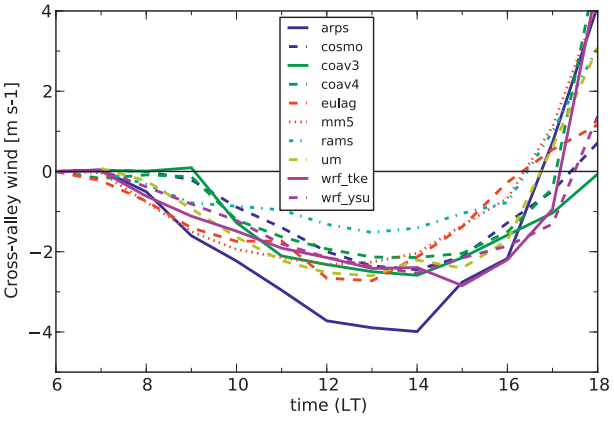

FIG. 4. Time series of cross-valley wind speed u at 100 m AGL over the western slope ($x = -6$ km, $y = 20$ km).

a *local* Deardorff-type TKE closure derived for large eddy simulations for which the length scale is based on the grid spacing (Deardorff 1980), and the final group (ARPS) uses a Deardorff-type closure but with a nonlocal determination of the length scale after Sun and Chang (1986). With respect to horizontal mixing/smoothing, several models (ARPS, COSMO, COAMPS, MM5, and UM) use fourth-order horizontal smoothing with a filter coefficient of $c_4 = 0.001\ \mathrm{s}^{-1}$, two models (RAMS and WRF-YSU) use a Smagorinsky-type scheme to parameterize horizontal mixing, and for two models (EULAG and WRF-TKE) horizontal mixing is parameterized as part of a three-dimensional turbulence closure. There are also large differences in the representation of the soil–surface–atmosphere coupling. In some models (COSMO, COAMPSv4, UM, and WRF) a distinct surface skin temperature is used, while in the other group (ARPS, COAMPSv4, EULAG, MM5, and RAMS) the surface temperature used in the surface energy budget is equal to the temperature of the uppermost soil layer. One group of models (ARPS, COSMO, COAMPSv3, COAMPSv4, RAMS, UM, and WRF) introduces additional resistances to the heat transfer between the surface and the atmosphere (e.g., roughness sublayer), while the other models (EULAG and MM5) couple the surface directly to the atmosphere using standard Monin–Obukhov similarity theory with equal roughness length for heat and momentum.

A common set of output variables with hourly resolution was defined, interpolated to a standard destaggered grid, and stored in a standardized Network Common Data Form (NetCDF) file format in order to make the simulation results easily comparable. The common set of variables includes the usual thermodynamic state variables and the variables required to calculate the surface radiation and energy budget (surface sensible and latent heat flux, net radiation and incoming and outgoing solar and longwave radiation components), soil temperature, and soil moisture variables.

c. Analysis method

As mentioned in the introduction, the surface sensible heat flux in combination with the valley volume effect is the primary driver of the thermally induced slope and valley winds. Clearly, the volume effect is identical for all models, thus any substantial differences among the models is likely be related to the simulation of the surface energy balance. The surface energy balance (SEB) can be written as (Bonan 2008)

$$R_n = (S_d - S_u) + (L_d - L_u) = H + \mathrm{LE} + G; \qquad (5)$$

it requires that the energy gained from net radiation R_n be balanced by the fluxes of sensible (H) and latent heat

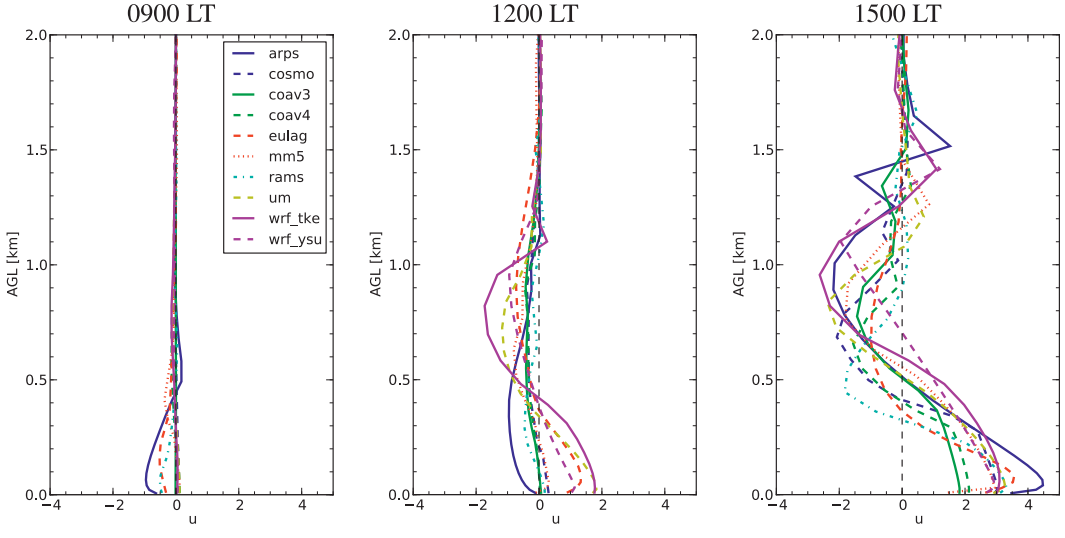

FIG. 5. As in Fig. 3, but over the western ridge ($x = -10$ km, $y = 20$ km).

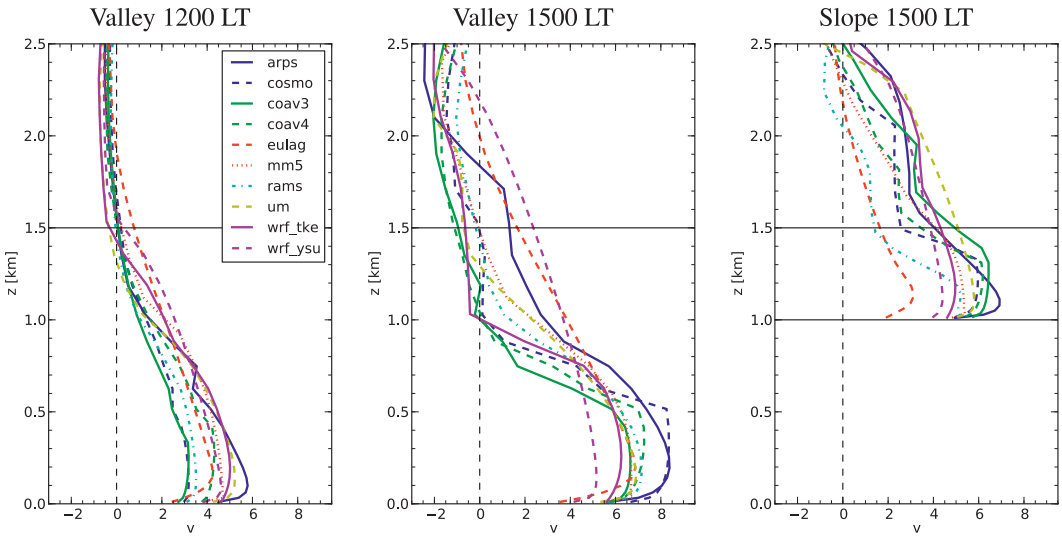

FIG. 6. Profiles of along-valley wind speed v at the valley center ($x = 0$ km) and over the western slope ($x = -6$ km). The along-valley position is $y = 20$ km.

(LE) to the atmosphere and the heat flux into the ground (G). Net radiation R_n is the sum of net solar radiation ($S_n = S_d - S_u$) and net longwave radiation ($L_n = L_d - L_u$), where the subscripts d and u refer to downwelling and upwelling radiation fluxes.

To better distinguish between differences among the models originating from the radiation scheme and those coming from the land surface scheme, we rewrite the energy balance, using $L_u = L_e + (1 - \epsilon)L_d$, to obtain

$$\underbrace{S_n + \epsilon L_d}_{Q_a} = H + \mathrm{LE} + G + L_e, \tag{6}$$

where Q_a is the total absorbed radiation, $L_e = \epsilon\sigma T_s^4$ is the longwave radiation emitted by the land surface, and ϵ represents the longwave emissivity of the surface (see Bonan 2008). Now all terms that depend on the surface temperature (T_s) are regrouped on the right-hand side of the equation. In a final step, we subtract an "inactive" longwave emission term, $L_{e0} = \epsilon\sigma T_{s0}^4$, corresponding to the emission of the soil at its initial temperature ($T_{s0} = 280$ K), from both sides of the equation to arrive at

$$Q_a' \equiv S_n + \epsilon L_d - L_{e0} \tag{7}$$

$$Q_a' = H + \mathrm{LE} + G + L_e', \tag{8}$$

where $L_e' = L_e - L_{e0}$ is the net emitted longwave radiation and Q_e' is the net absorbed radiation. Equation (7) represents the radiative forcing of the land surface, which is determined by the radiation scheme, while the fluxes in (8) are strongly influenced by surface temperature and are determined by the land surface scheme.

3. Results

A detailed comparison of the simulated valley wind system for the nine mesoscale models is given in this section. We start out with a comparison of the evolution of the local flow and the mean along-valley wind, followed by a detailed analysis of model differences in terms of their simulation of the surface energy fluxes and the discussion of some sensitivity experiments. It should be noted that the general evolution of the valley wind system is qualitatively similar to previous idealized studies (e.g., Li and Atkinson 1999; Rampanelli et al. 2004; Schmidli and Rotunno 2010) and the reader is referred to these studies for an interpretation of the simulations in terms of valley wind theory.

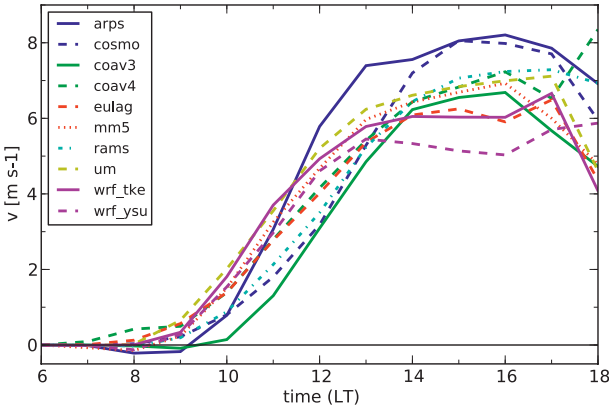

FIG. 7. As in Fig. 4, but for the along-valley wind speed v at the valley center ($x = 0$ km) at 100 m AGL. The along-valley position is $y = 20$ km.

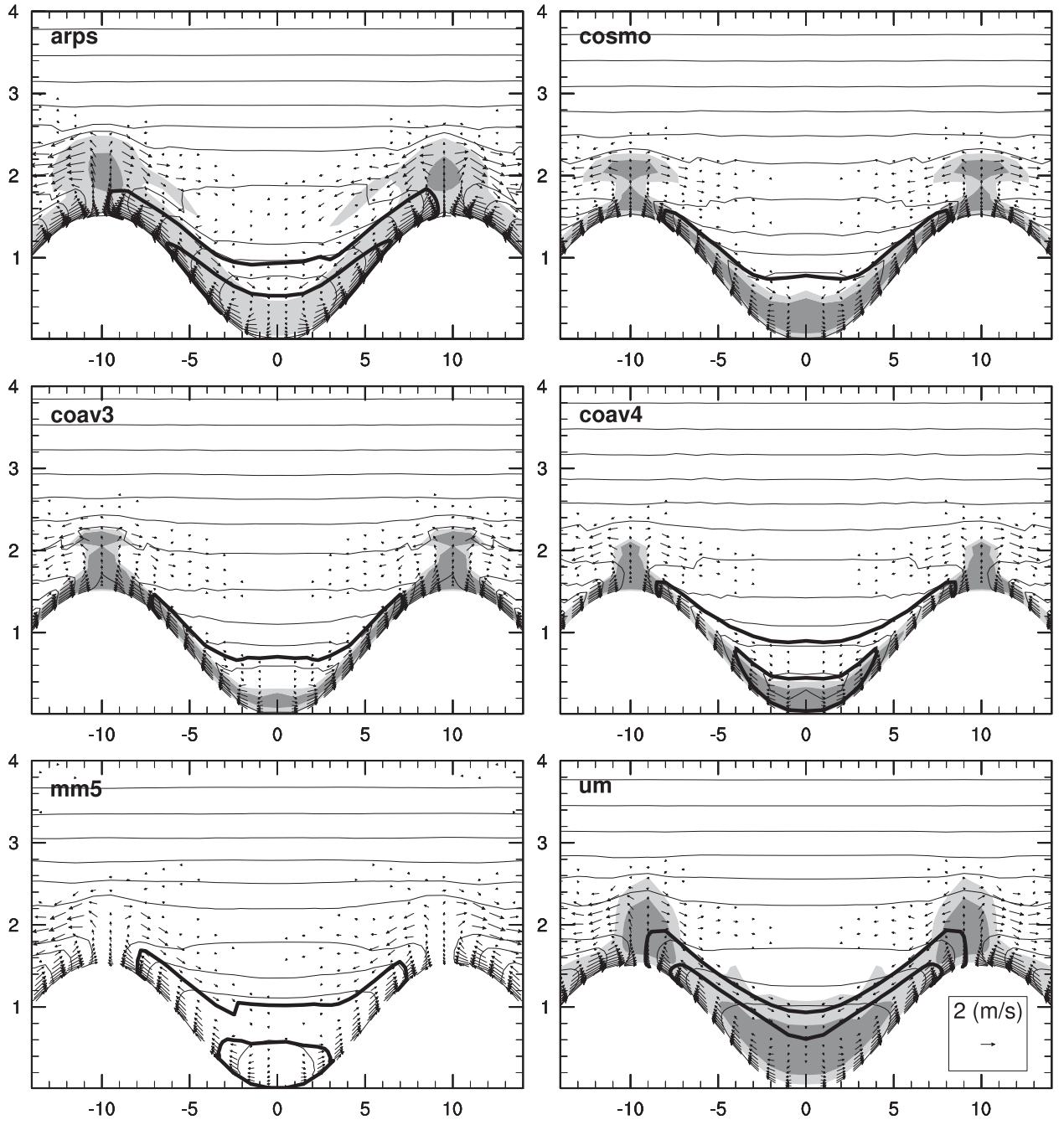

FIG. 8. Snapshot of the flow at 1200 LT in the west–east cross section at $y = 20$ km. Along-valley wind component (thick bold lines; contour interval 2 m s^{-1}), potential temperature (thin lines; contour interval 1 K), cross-valley circulation (vectors), and vertical diffusion coefficient (shading; 10 and 50 m^2 s^{-1}; not available for MM5, WRF-YSU, EULAG, and RAMS). The axis units are in km.

a. Local evolution

1) BOUNDARY LAYER EVOLUTION

Figure 2 compares potential temperature profiles from the various models at 1200 LT at the four sites shown in Fig. 1. A typical convective boundary layer (CBL) has developed over the plains at this time, with mixed layer (ML) depths ranging from 600 m for RAMS to 1200 m for WRF-YSU, and ML potential temperatures in the range of 285–288 K. A well-mixed CBL has also developed over the mountain ridge, with ML depths ranging from 400 to 1000 m. A more complex temperature structure has developed at the two valley sites (valley and slope). The valley center site shows the typical three-layer

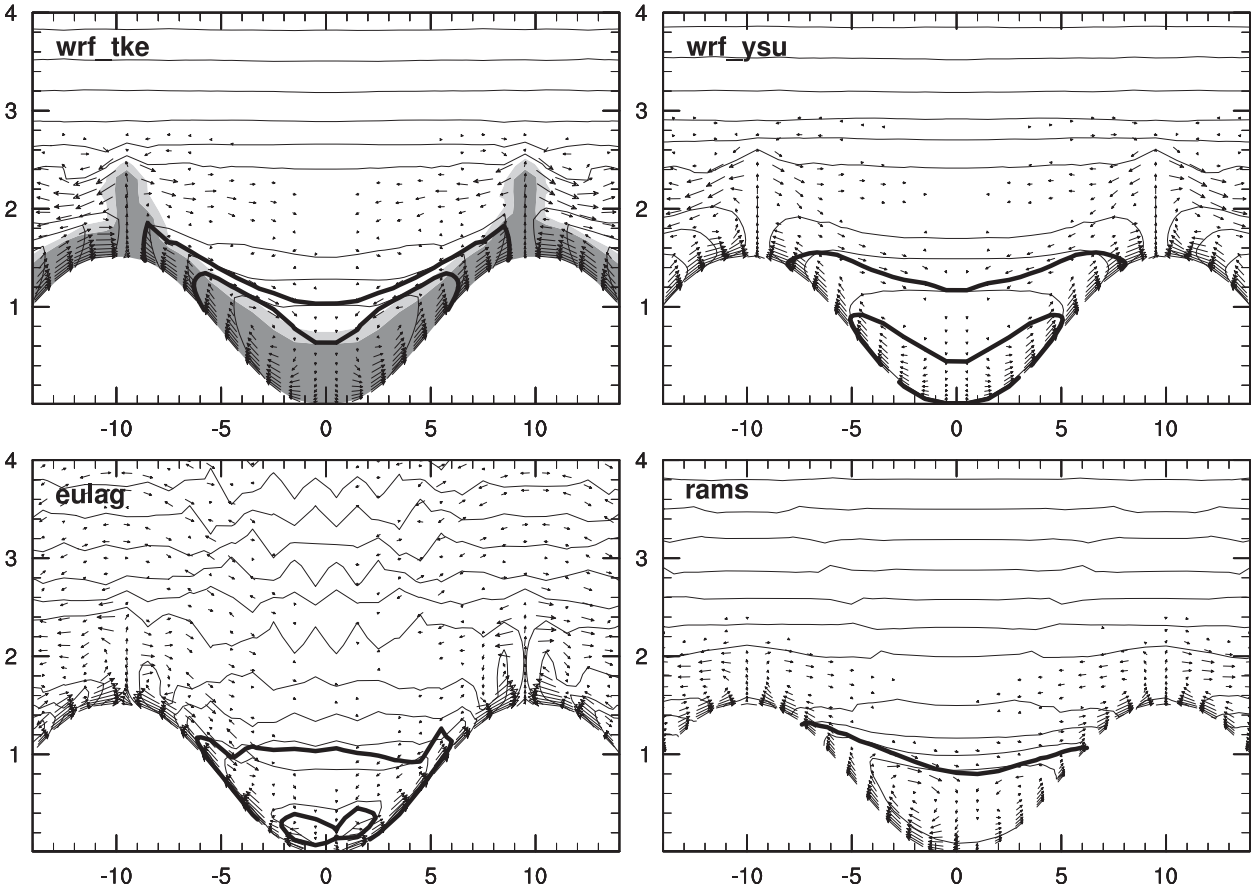

FIG. 8. (*Continued*)

structure found in many mountain valleys (Brehm 1986; De Wekker et al. 2005; Weigel et al. 2006), with a well mixed layer near the ground separated by a stable layer from a second nearly neutral layer aloft. There are large differences in the simulated potential temperature structure between the models. The depth of the ML ranges from 300 (COAMPSv3) to 1300 m (WRF-YSU); the height of the lower boundary of the upper neutral layer varies between 1200 (COAMPSv3) and 1700 m (WRF-YSU). The soundings over the valley slope exhibit a similar structure to the valley center site, but with a less marked stable layer, and with somewhat less variation among the models.

2) CROSS-VALLEY CIRCULATION

Figure 3 depicts vertical profiles of the cross-valley wind speed over the western slope at $x = -6$ km at 0900, 1200, and 1500 LT. Note that because of the small slope angles involved (maximum slope angle is 14.6°), the cross-valley u component of the wind and the tangential along-slope wind speed differ by less than 3%. The differences among the models are relatively small in the morning, but quite large in the afternoon. The depth of the upslope wind layer grows from about 200 m at 0900 LT, to 300–500 m at 1200 LT, to over 500 m in some models in the afternoon. Note also the onset of the plain-to-mountain wind (east–west wind) about 500 m above ridge height in the 1200 and 1500 LT soundings, and the large variability among the models in the simulated strength and structure of this wind, especially in the afternoon.

The time evolution of the upslope wind at 10 m AGL on the western slope at $x = -6$ km is shown in Fig. 4. The wind starts soon after sunrise and increases in strength until noon/early afternoon. The simulated evolution is initially quite similar for most models, although there are quite substantial differences in the timing of the onset of the upslope flow. In the afternoon the models differ by more than 2 h in the timing of the reversal to downslope flow, with the transition to downslope flow occurring first in models that include slope-dependent solar radiation (EULAG, MM5, and RAMS; see Table 2).

3) PLAIN-TO-MOUNTAIN CIRCULATION

The plain-to-mountain circulation is clearly visible in Fig. 5, which depicts vertical profiles of the cross-ridge

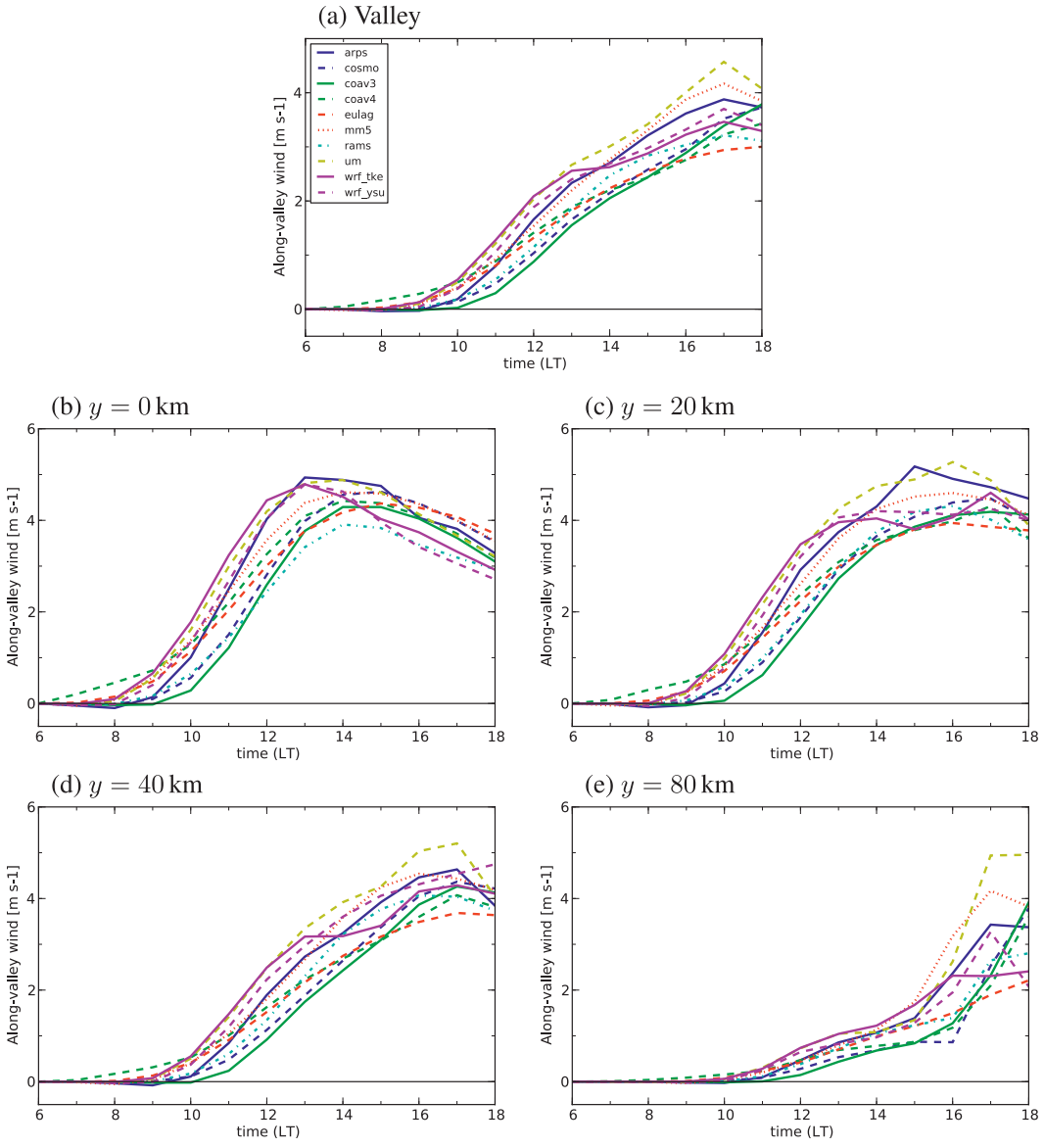

FIG. 9. Time series of mean along-valley wind speed v: (a) averaged over the entire valley ($-10 \le x \le 10$ km, $0 \le y \le 100$ km, $0 \le z \le 1500$ m); (b)–(e) averaged over the valley cross-section at different along-valley locations.

wind over the western ridge. By 1200 LT, there is a plain-to-mountain flow at $x = -10$ km in the lowest few hundred meters for several models (UM, WRF, and EULAG) and a return mountain-to-plain flow in a layer extending from about 500 to 1200 m above ground. The other models exhibit either very weak winds (COSMO, COAMPSv3, COAMPSv4, MM5, and RAMS) or a mountain-to-plain wind (ARPS) at this particular location. This apparently large difference among the models is the result of minor differences in the exact location of the convergence point on top of the mountain ridges between the opposing upslope flows. By 1500, there is a plain-to-mountain circulation in all models, but with large differences in its vertical structure.

4) ALONG-VALLEY FLOW

Figure 6 shows vertical profiles of the along-valley wind at 1200 and 1500 LT over the valley center and the western slope. At 1200 LT there is relatively good agreement in the qualitative structure of the vertical profile of the simulated along-valley wind among the models. The differences in the maximum up-valley wind speed, however, are already quite large and range from 3 to 6 m s^{-1}, and the depth of the up-valley wind layer

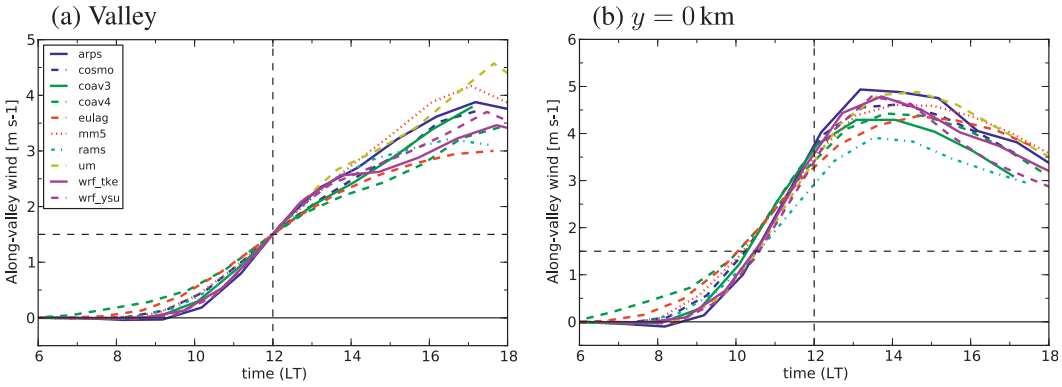

FIG. 10. As in Fig. 9, but with synchronization of model evolution at 1200 LT through time shifting of individual model curves such that $\overline{v}(1200\,\mathrm{LT}) = 1.5\,\mathrm{m\ s^{-1}}$.

varies between 1200 and 1800 m. At 1500 LT there are substantial differences among the models in the vertical structure of the simulated along-valley wind. The depth of the up-valley wind layer varies from 1000 m for COAMPSv3, COAMPSv4, COSMO, and WRF-TKE to over 2000 m for EULAG and WRF-YSU. For most models, the up-valley wind speed at the slope site is much larger than at the corresponding height over the valley center, suggesting that the up-valley momentum is advected upslope by the slope flows.

The time evolution of the along-valley wind at 100 m AGL for the valley center is shown in Fig. 7. Initially there is quite good agreement among the models, apart from a time shift. This changes rapidly, however, after noon. In the late afternoon, the simulated wind speeds vary by more than 3 m $\mathrm{s^{-1}}$.

5) SPATIAL STRUCTURE

The spatial structure of the simulated along-valley wind together with the cross-valley circulation at 1200 LT is

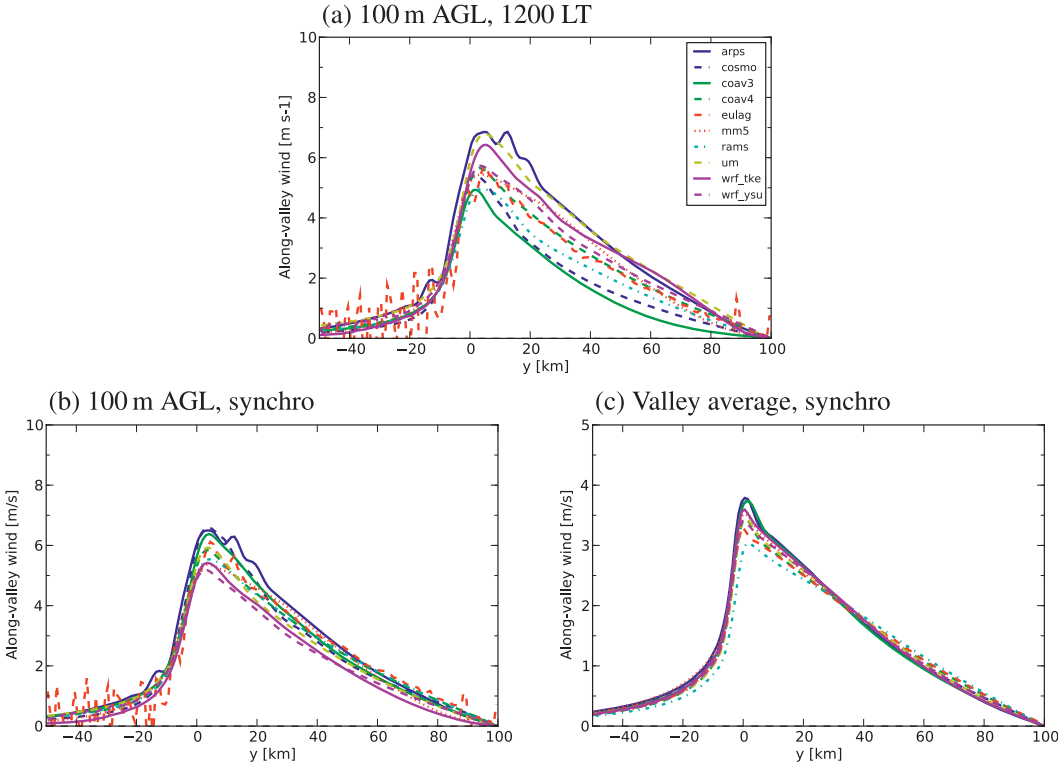

FIG. 11. Along-valley variation of the along-valley wind speed at 1200 LT and synchronized as in Fig. 10: (a) 1200 LT at $x = 0$ km, $z = 100$ m; (b) synchronized at $x = 0$ km, $z = 100$ m; (c) synchronized and averaged over valley cross section ($-10 \le x \le 10$ km, $0 \le z \le 1500$ m).

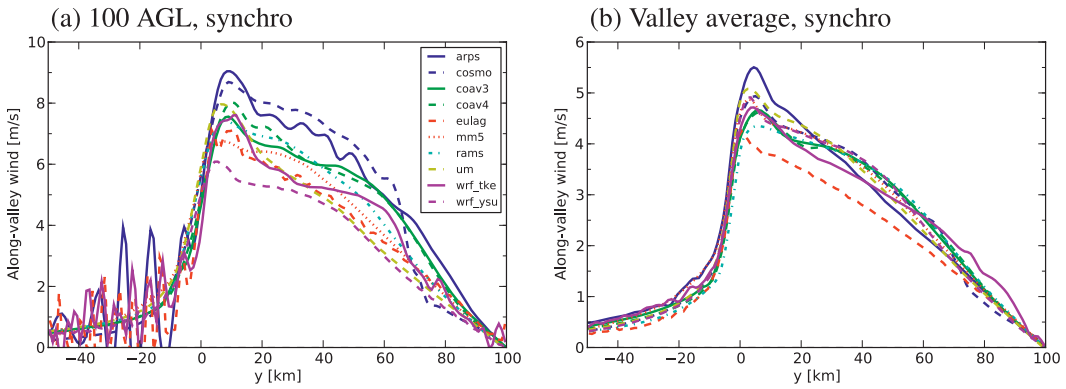

FIG. 12. As in Fig. 11, but for 1500 LT and resynchronized such that $\overline{v} = 2.75\,\mathrm{m\,s^{-1}}$ at 1500 LT.

shown in Fig. 8. The cross-valley circulation is well established with upslope flows on all slopes, flow convergence over the mountain ridges, and weak subsidence over the center of the valley. The depth of the upslope flow layer varies by more than a factor of 2 between the shallow results with the COAMPS models and the deeper results with UM and WRF-YSU. There is also considerable variation in the structure of the return flow, which is approximately parallel to the slope for MM5, but closer to horizontal for many of the other models. The depth of the up-valley flow layer in the valley center is quite shallow for the two COAMPS models and COSMO, but it extends almost to the height of the mountain ridges for many of the other models. There is also considerable variation in the strength and spatial structure of the up-valley flow. The main cause of the difference in the depth of the slope wind layer and the up-valley flow among the models is likely due to the turbulence parameterization. The models using a scheme based on the *K*-profile method (UM and WRF-YSU) tend to simulate the deepest boundary layers. Another characteristic difference among the models is the tendency to a broader convergence zone over the mountain ridge for the models that use computational horizontal mixing (see Table 1). This finding is confirmed by additional simulations with the same model (WRF-YSU) but different settings for horizontal diffusion (e.g., no horizontal mixing, Smagorinsky-type mixing, and computational horizontal mixing; not shown).

b. *Mean along-valley flow*

The previous section showed substantial differences in the local evolution of the valley wind system among the models. These differences at the local scale can be thought to originate from two sets of factors: those related to the bulk evolution of the flow and those specific to the local structure such as horizontal and vertical mixing. In the following we try to distinguish between these sets of factors by analyzing the bulk evolution of the flow and by developing a synchronization procedure (see below).

The evolution of the mean along-valley wind, averaged over the entire valley volume, is shown in Fig. 9a. It is clear that the differences are smaller than the differences for the along-valley wind at any specific location (cf. to Fig. 7). There is a notable time shift in the onset and evolution of the mean along-valley wind among the models. A similar time shift is then found for the along-valley wind at different along-valley positions (Figs. 9b–e).

We introduce a synchronization procedure in order to compensate for differences among the models, which are due only to a time shift in the bulk evolution of the valley flow. The procedure is based on the valley-mean valley wind (Fig. 9a). The time shift for each model is determined by moving the individual model curves such that the valley-mean valley wind equals $1.5\,\mathrm{m\,s^{-1}}$ at 1200 LT. For the two extremes, WRF-TKE and COAMPSv3, this means shifting the time axis by +43 min for WRF-TKE and by −55 min for COAMPSv3. The resulting synchronized evolution of the valley-mean along-valley flow is shown in Fig. 10a. Although the overall evolution of the along-valley flow is remarkably similar among the models, significant differences in the speed-up of the along-valley wind are apparent. Similar differences are also seen for the mean along-valley wind at the valley entrance (Fig. 10b).

Synchronization and the difference between local and bulk flow properties is further illustrated in Fig. 11, which shows the along-valley variation of the along-valley flow. At the local scale (100 m AGL, Fig. 11a) the differences among the models are large, up to $2\,\mathrm{m\,s^{-1}}$ at any specific location. Synchronization significantly reduces the differences among the models (Fig. 11b), to about $1\,\mathrm{m\,s^{-1}}$. The synchronized bulk along-valley flow (i.e., the along-valley flow averaged over the valley cross section, is very similar for all models; Fig. 11c). This result is quite remarkable. Despite large differences in the detailed spatial

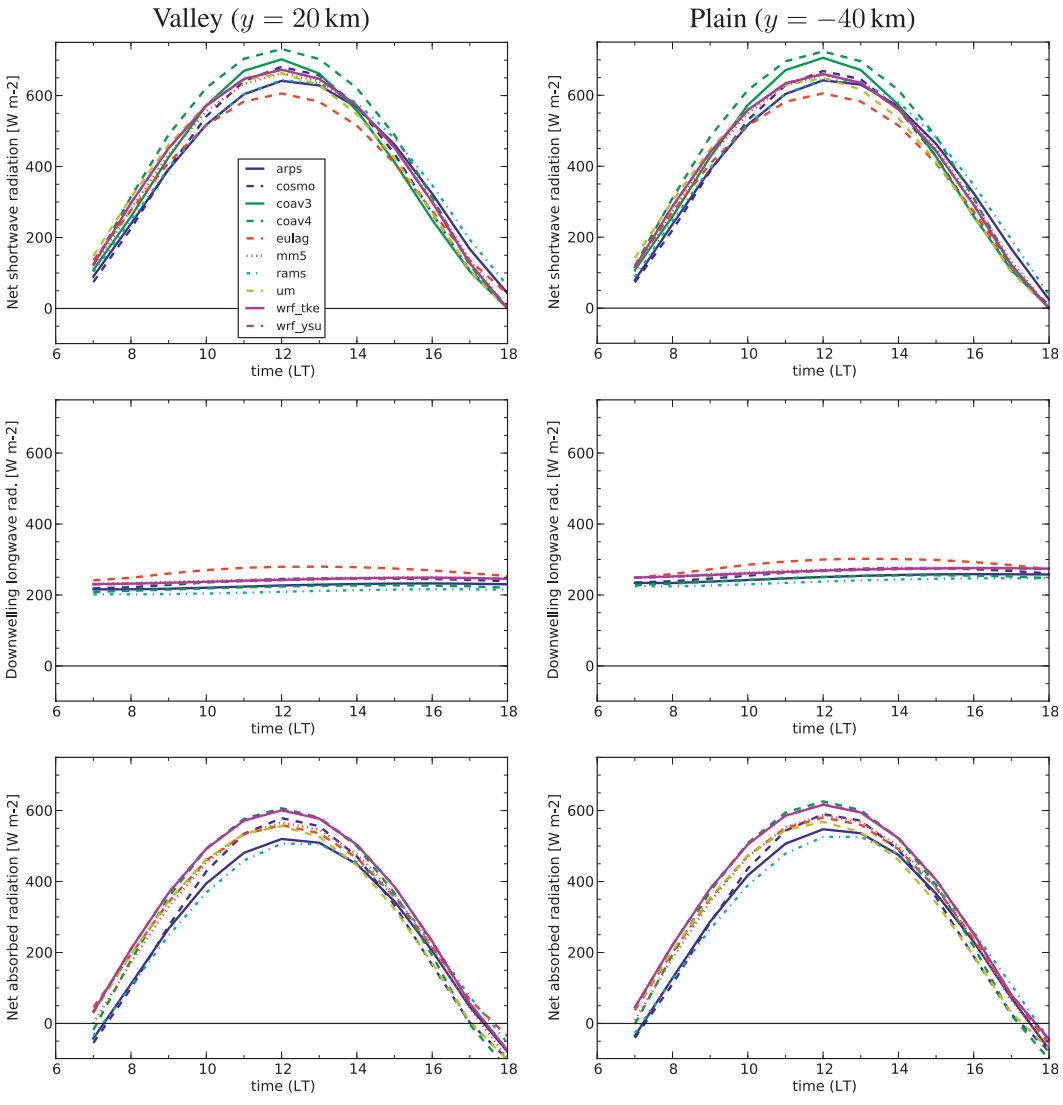

FIG. 13. Time series of net shortwave radiation S_n, downwelling longwave radiation L_d, and net absorbed radiation at the surface Q_a', averaged over $-10 \le x \le 10$ km.

structure of the simulated valley wind system (Fig. 8), the bulk flow evolution is almost identical in all models, at least until 1200 LT. Regarding the spatial structure of the flow, note the high-frequency oscillation of the along-valley wind speed over the plain and near the valley end for EULAG. These oscillations may be associated with unresolved cellular motions in the boundary layer.

Three hours later, the local differences among the models are much larger, even when resynchronized such that $\overline{v} = 2.75\,\mathrm{m\,s^{-1}}$ at 1500 LT (Fig. 12a). High-frequency oscillations due to cellular motions in the convective boundary layer over the plain are now also visible for ARPS and WRF-TKE. Again, the spread among the models is much reduced for the bulk along-valley flow (Fig. 12b), but the curves do not collapse as well as at 1200 LT.

In summary, during an early phase, the evolution of the bulk along-valley flow is almost identical for all models, apart from differences in the speed of the evolution. During a later phase, there are genuine differences among the models also in the along-valley structure of the bulk along-valley flow.

c. *Sensible heat flux, surface energy balance, and valley wind evolution*

Valley wind theory suggests that differences among the models in the bulk evolution of the flow, at least during an early phase, is related to differences in the evolution of the surface sensible heat flux among the models (e.g., Schmidli and Rotunno 2010). Thus, differences in the

TABLE 3. Surface energy fluxes averaged over 0630–1230 LT, for a valley location ($-10 \le x \le 10$ km, $y = 15 \ldots 25$ km). All fluxes are in W m^{-1}. Listed quantities include: downwelling solar radiation (S_d), net solar radiation (S_n), downwelling longwave radiation (L_d), net absorbed radiation (Q'_a), longwave surface emissivity (ϵ), sensible heat flux (H), latent heat flux (LE), ground heat flux (G), net longwave emission (L'_e), the fraction of incoming solar radiation converted to net absorbed radiation, $\sigma_{\text{rabs}} = Q'_a/S_d$, and the fraction of net absorbed radiation converted to sensible heat flux $\sigma_{\text{shf}} = H/Q'_a$. COAMPSv3 was not included for the calculation of the mean and the standard deviation as not all required radiation components were available.

Model	S_d	S_n	L_d	Q'	σ_{rabs}	ϵ	H	LE	G	L'_e	σ_{shf}
ARPS	567	414	220	289	0.51	0.98	174	7	69	39	0.60
COSMO	541	426	232	310	0.57	1.00	121	0	158	31	0.39
COAMPSv3	-	456	-	-	-	-	153	40	-	23	6.78
COAMPSv4	681	497	217	365	0.54	1.00	142	2	196	25	0.39
EULAG	577	422	263	356	0.62	0.85	191	0	114	51	0.54
MM5	612	446	238	343	0.56	0.95	184	55	87	16	0.54
RAMS	576	419	204	276	0.48	0.99	147	10	107	12	0.53
UM	639	467	235	354	0.55	1.00	191	32	95	36	0.54
WRF-TKE	631	461	236	360	0.57	0.92	245	5	90	39	0.68
WRF-YSU	631	461	236	361	0.57	0.92	209	5	110	57	0.58
Mean	606	446	231	3335	0.55	0.96	178	13	114	34	0.53
Std dev	42	26	15	32	0.04	0.05	35	17	37	14	0.09
Std dev (%)	7	6	7	10	7	5	20	136	33	41	17

surface energy balance among the models are analyzed next using the concepts outlined in section 2c.

Figure 13 shows the time evolution of selected radiation fluxes at the surface for a valley ($y = 20$ km) and a plain location ($y = -40$ km). The fluxes are averaged over the width of the valley for both locations (i.e., $-10 \le x \le 10$ km). Corresponding time-averaged surface energy fluxes for the morning period 0630–1230 LT are given in Tables 3 and 4. As expected, all models show a similar evolution of net solar radiation S_n but with notable differences in magnitude. Despite almost identical atmospheres, average net solar radiation varies between 414 and 497 W m^{-2} for the valley location (Table 3). The standard deviation for S_n is equal to 26 W m^{-2} or 6% of the model mean. For downwelling longwave radiation L_d, the absolute differences among the models are smaller, although of comparable relative magnitude. The differences in the magnitude of net absorbed radiation, Q'_a, among the models translate into an apparent time shift of the radiative forcing of up to 1 h during the morning hours.

The partitioning of the net absorbed radiation Q'_a into the surface heat fluxes (H, LE, G) and the longwave emission L'_e is illustrated in Fig. 14. Again time-averaged fluxes are given in Tables 3 and 4. Clearly, the uncertainties increase with the step from net absorbed radiation to surface sensible heat flux. The relative differences among the models for the valley location increase from 10% to 20% (Table 3), and the apparent time shift between the ''fastest'' and ''slowest'' model increase to up to 2 h (Fig. 14). Similar differences are found for the plain location. As can be seen from Fig. 14, all components of the surface energy balance contribute to the large variations among the models. Clearly, the largest single factor is the ground heat flux. There are

TABLE 4. Surface energy fluxes averaged over 0630–1230 LT, for a plain location ($-10 \le x \le 10$ km, $y = -45 \ldots -35$ km), as in Table 3. The fraction of valley-to-plain sensible heat flux is denoted as $r_{\text{shf}} = H_{\text{valley}}/H_{\text{plain}}$.

Model	S_d	S_n	L_d	Q'	σ_{rabs}	ϵ	H	LE	G	L'_e	σ_{shf}	r_{shf}
ARPS	562	411	241	308	0.55	0.97	120	10	110	69	0.39	1.45
COSMO	530	418	251	321	0.61	1.00	111	0	167	42	0.35	1.09
COAMPSv3	-	457	-	-	-	-	128	45	-	41	3.12	1.20
COAMPSv4	673	491	240	382	0.57	1.00	122	2	210	48	0.32	1.16
EULAG	571	417	277	365	0.64	0.85	160	0	139	66	0.44	1.19
MM5	602	440	261	358	0.59	0.95	148	61	115	34	0.41	1.24
RAMS	573	416	230	293	0.51	1.03	136	1	130	26	0.46	1.08
UM	623	455	258	365	0.59	1.00	150	42	114	59	0.41	1.27
WRF-TKE	615	449	259	371	0.60	0.92	220	7	105	60	0.56	1.11
WRF-YSU	615	449	258	372	0.60	0.92	181	6	126	80	0.46	1.15
Mean	596	438	253	348	0.58	0.96	150	14	135	54	0.43	
Std dev	40	25	13	30	0.04	0.05	32	21	32	17	0.08	
Std dev (%)	7	6	5	9	6	6	22	144	24	31	18	

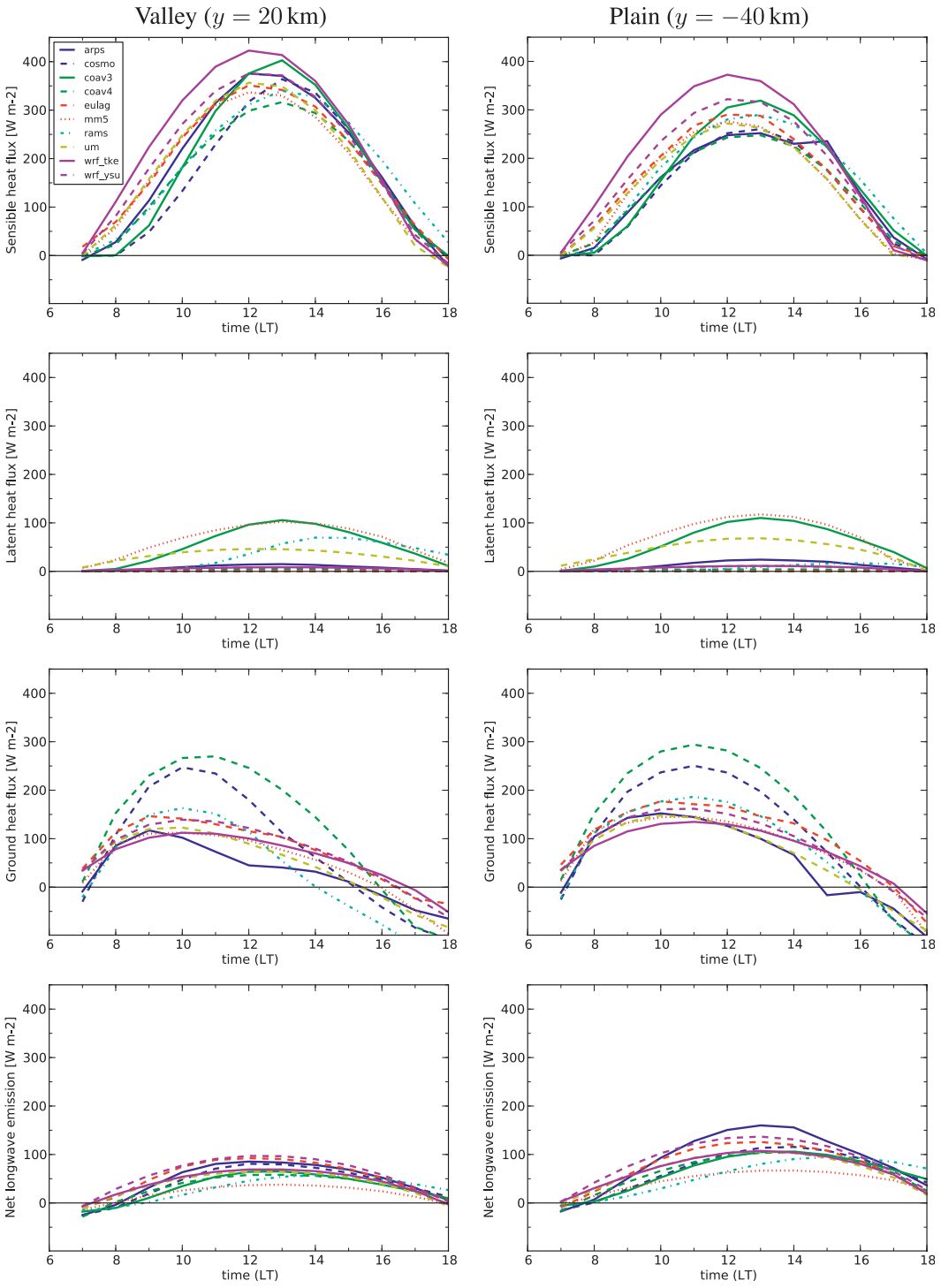

FIG. 14. As in Fig. 13, but for the sensible heat flux H, the latent heat flux LE, the ground heat flux G, and net longwave emission L_e'.

large variations in its temporal evolution and the maximum value varies by more than a factor of 2 among the models. The differences in the latent heat flux and longwave emissions are smaller, but still substantial. Note that the differences in the longwave emission L_e' are a reflection of the differences in the surface (skin) temperature among the models. A concise summary of these results for the morning period 0630–1230 LT is

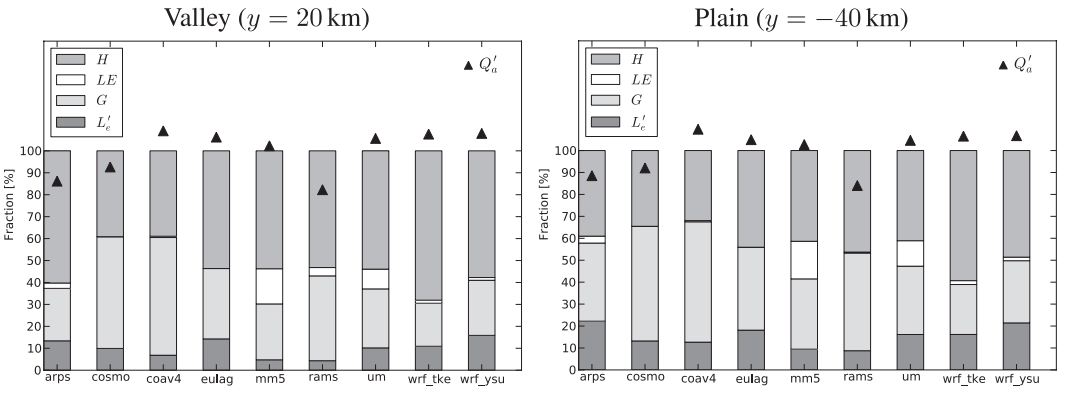

FIG. 15. Partitioning of the net absorbed energy Q'_a into sensible heat flux H, latent heat flux LE, ground heat flux G, and net longwave emission L'_e: (left) valley and (right) plain. The surface energy fluxes are averaged over 0630–1230 LT. The triangles show the relative variation of Q'_a among the models (model mean equals 100).

presented in Fig. 15. Again large variations among the models are visible in the relative partitioning of net absorbed energy Q'_a into its components. Extending the averaging period until late afternoon (0630–1530 LT) does not substantially change the picture, apart from a slight increase of the sensible heat flux H (5% points, on average) and the longwave emission L'_e fraction (3% points) at the expense of the ground heat flux fraction.

The large differences in the evolution of the surface sensible heat flux are then translated into corresponding differences in the evolution of the potential temperature in the valley and over the plain (Fig. 16). Note that there is not a one-to-one correspondence between the evolution of the sensible heat flux and the potential temperature, as not only the heat input into the valley control volume, but also the heat loss due to advective and turbulent transport differs among the models, in particular during the later phase of the development (not shown). Furthermore, the evolution of the sensible heat flux and potential temperature not only differs among the models, but also between the valley and the plain location for any given model. The valley–plain contrast of the integrated sensible heat flux, $r_{\mathrm{shf}} = H_{\mathrm{valley}}/H_{\mathrm{plain}}$, varies between 1.08 (RAMS) and 1.45 (ARPS) for the period 0630–1230 LT (see Table 4). All these factors lead to differences in the along-valley pressure gradient and the evolution of the valley wind.

It should be noted that the temporal evolution of the sensible heat flux and its spatial variation are the result of complex interactions among several model components including the radiation scheme, the soil model, the surface layer scheme, the boundary layer turbulence scheme, and the valley wind system. The large variation among models of a key surface layer relation—the dependence of the drag and heat transfer coefficient on wind speed—is illustrated in Fig. 17. For weak winds the transfer coefficients vary by more than an order of magnitude among the models and even for strong winds (larger than 5 m s^{-1}) the variation still exceeds a factor of 2. These and other factors then determine the conversion efficiency from radiation absorbed at the surface

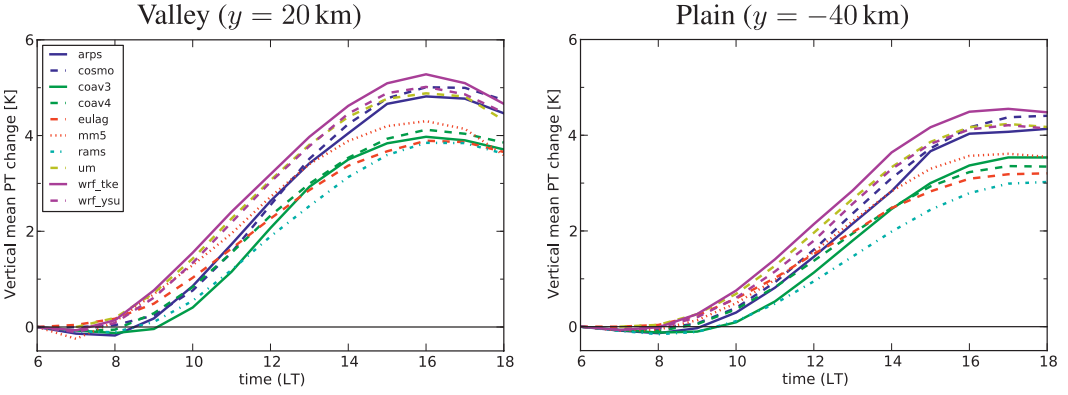

FIG. 16. Time series of the vertically averaged potential temperature change (average from the surface to 1500 m) at $x = 0$ km: (left) valley and (right) plain.

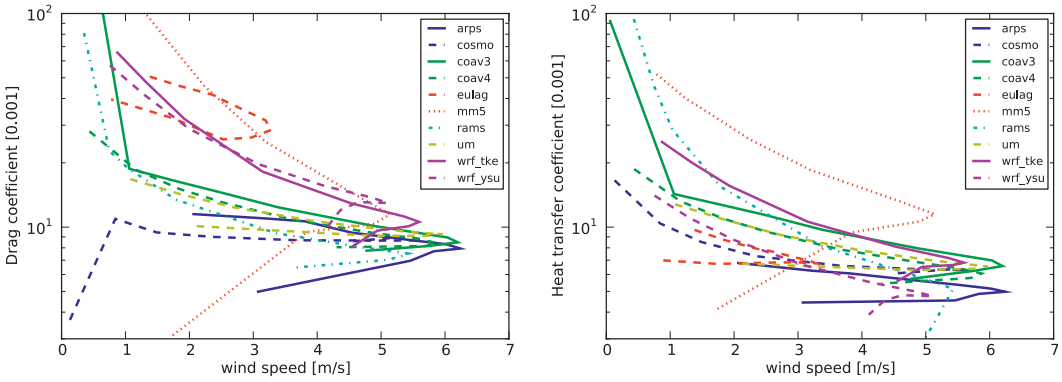

FIG. 17. Variation of (left) the drag coefficient and (right) the heat transfer coefficient as a function of wind speed for a valley location ($x = -6$ km and $y = 20$ km).

to surface sensible heat flux, the primary driver of the thermally induced slope and valley winds.

d. Sensitivity experiments

In this section, we briefly examine the sensitivity of the evolution of the valley wind system to the type and magnitude of horizontal and vertical mixing. Characteristic results with regard to the evolution of the bulk flow are shown in Fig. 18 for two of the models: ARPS and WRF. The evolution of the bulk flow is almost independent of the detailed settings. Changing the horizontal mixing coefficient by an order of magnitude, changing the type of horizontal mixing (fourth-order computational mixing, Smagorinsky-type mixing, or no horizontal mixing), or changing the turbulence mixing coefficient c_t in the TKE closure in ARPS by a factor of 2 (by increasing c_t in $K = c_t E^{1/2} l$ from 0.1 to 0.2) has almost no influence on the simulated evolution of the bulk along-valley wind. Even changing the turbulence parameterization scheme (WRF) or the horizontal grid spacing (ARPS) has only a minor influence on the simulated bulk flow evolution.

Typical results with regard to the influence of horizontal mixing on the spatial structure of the flow are shown in Fig. 19. As expected, the flow is less smooth for the simulation with a small horizontal mixing coefficient. Further differences include a tendency to a more narrow convergence zone of the upslope flows and a slightly faster downslope propagation of the plain-to-mountain flow in the afternoon for the reduced mixing simulation. Although the differences between the two simulations at any specific location might be substantial, the overall qualitative flow structure is nevertheless very similar.

In summary, horizontal mixing has little effect on the physical aspects of the flow such as boundary layer depth and the evolution of the bulk flow. Its main effect is on the smoothness of the fields. Vertical mixing and the

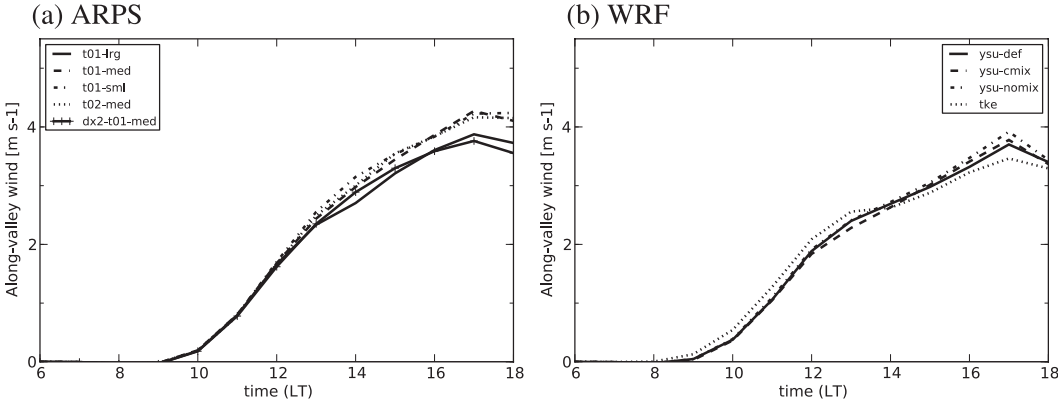

FIG. 18. Sensitivity of simulated mean along-valley wind to horizontal diffusion and turbulence mixing for 2 selected models. (a) ARPS: Variation of the fourth-order horizontal mixing coefficient lrg (0.001 s^{-1}), med (0.000 25 s^{-1}), sml (0.0001 s^{-1}), the vertical mixing coefficient of the turbulence scheme, t01 (0.1), t02 (0.2), and the horizontal grid spacing dx2 ($\Delta x = 2$ km). (b) WRF: Variation of horizontal mixing, def (Smagorinsky), cmix (fourth-order horizontal mixing), and nomix (no horizontal mixing), and the turbulence scheme (ysu vs tke).

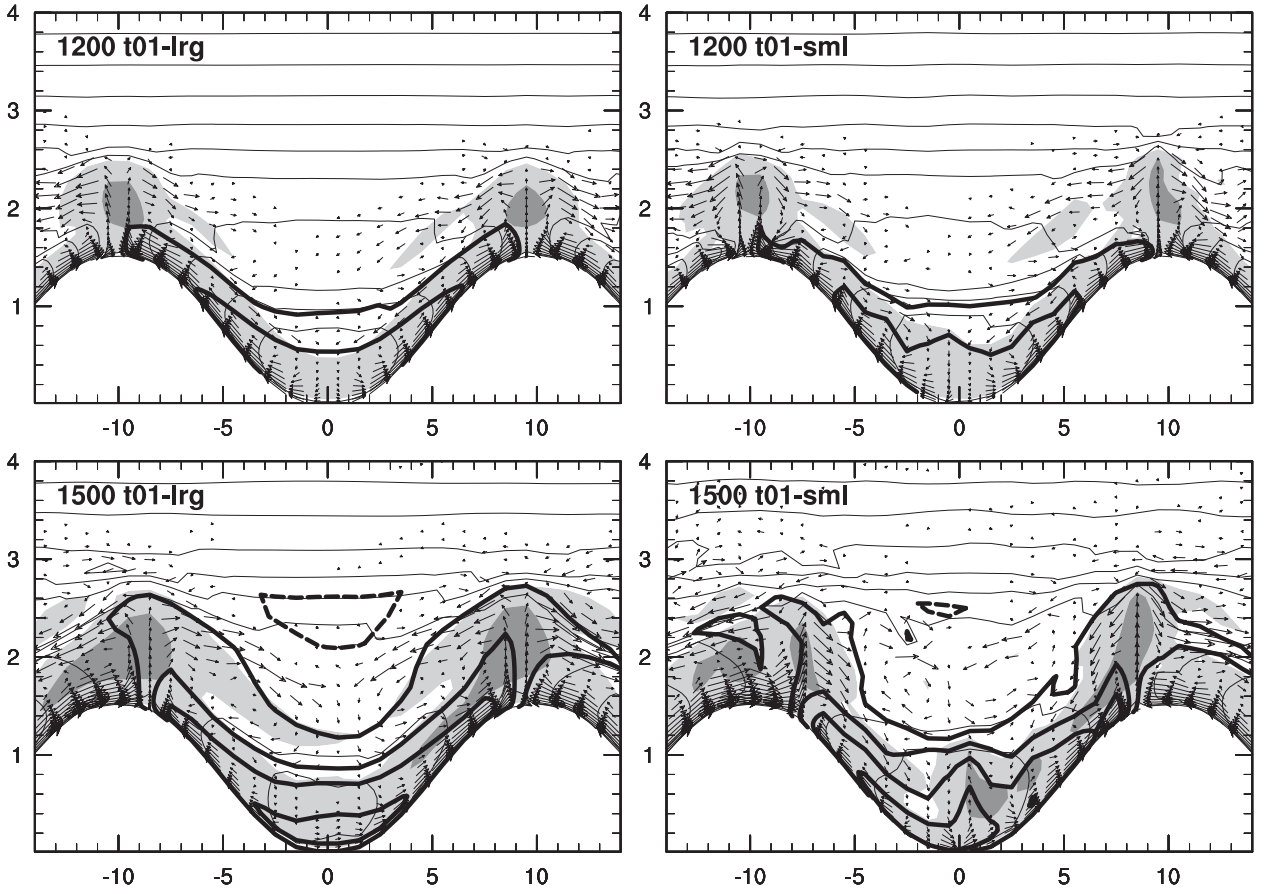

FIG. 19. As in Fig. 8, but for ARPS sensitivity runs. Abbreviations as in Fig. 18.

choice of turbulence scheme also has little effect on the evolution of the bulk flow (Fig. 18), but it does have a major influence on the vertical structure of the flow, such as the depth of the boundary layers (see, e.g., the two WRF configurations in Fig. 6) and the near-surface values of temperature and wind. Similar strong sensitivity of boundary layer structures and near-surface fields on the choice of turbulence schemes has been documented in several previous studies (e.g., Zhong and Fast 2003; Zhang and Zheng 2004; Berg and Zhong 2005; Zängl et al. 2008; Hu et al. 2010).

4. Summary and conclusions

We have presented a detailed intercomparison of nine mesoscale models that are applied to simulate the evolution of the coupled boundary layer–valley wind system for an idealized valley–plain configuration.

All models produce a qualitatively similar evolution of the valley wind system with a strong up-valley flow. The temporal evolution of the valley-mean up-valley wind is similar for all models, except for differences in timing. After time synchronization, the along-valley variation of the cross-section-mean up-valley wind is almost identical for all models during the early phase of the valley-wind evolution, but significant differences start to develop after midday. With regard to spatial structure significant differences are found among the models, especially with regard to the vertical structure of the boundary layers, the vertical profile of the along-valley wind, and the occurrence or not of cellular motions in the convective boundary layer over the plain.

The largest source of uncertainty for the simulation of the mean along-valley wind is related to the parameterization of the soil–surface–atmosphere interaction and the radiation transfer scheme. The turbulence parameterization scheme is found to have a minor influence on the evolution of the averaged quantities, and the influence of the dynamical core and horizontal mixing is likely negligible. As a result of the strong coupling between the different model components (e.g., soil heat conduction, surface–atmosphere exchange, and flow dynamics) the last statement is, however, difficult to prove without

transferring the different parameterization schemes among the models.

Following the forcing chain, the most important factors leading to differences in the onset and speed of the temporal evolution of the mean along-valley wind are the following: incoming solar radiation at the surface; downwelling longwave radiation; partitioning of net absorbed radiation into sensible heat flux, latent heat flux, ground heat flux, and emitted longwave radiation; and dependence of the surface momentum and heat transfer coefficients on wind speed, in particular, for zero and weak-wind conditions. The largest single factor responsible for major differences is the ground heat flux.

With regard to the spatial structure of the simulated flow, the most important model component is the turbulence parameterization scheme. It has a significant influence on the vertical structure of the along-valley flow and of the boundary layers. Strong horizontal mixing results in smoother fields and may be responsible for the suppression of cellular motions in some models, but otherwise its influence is relatively small.

The simulation of the thermally driven valley wind system using an idealized valley–plain topography is a very useful test of mesoscale numerical models with respect to soil–surface–atmosphere interactions. Such simulations test the interaction of several important model components including the radiation transfer scheme, the soil model, the soil–vegetation–atmosphere transfer scheme, the boundary layer turbulence scheme, and the dynamical core of the model. While clouds and moist processes did not play any significant role in the present study, they surely would be a further major source of uncertainty in most real-case situations and it would be of interest to include the effect of significant soil moisture, clouds, and moist convection in future studies. On the other hand, the large differences with respect to the local evolution of the flow, particularly near the surface, point to the need for further investigation of the interaction between parameterized turbulence and thermally induced flows even without the complicating influences of moisture.

Acknowledgments. The first author acknowledges the Swiss National Science Foundation Grant PA002-111427 and the Center for Analysis and Prediction of Storms, University of Oklahoma, for access to and support of the ARPS model. Several of the authors acknowledge NSF Grants ATM-06545784 (Chow), ATM-0524891 (Grubisić), ATM-0524891 (Jiang), ATM-0444205 (Schmidli), ATM-0521776 and ATM-0837870 (Whiteman); NSF MRI Grants CNS-0421498, CNS-0420873, and CNS-0420985 (Wyszogrodzki); and ONR Grants PE 0601153N (Doyle and Holt). EULAG's computer time was supported in part by NSF sponsorship of the National Center for Academic Research, the University of Colorado, and a grant from the IBM Shared University Research (SUR) program. COAMPS(r) is a registered trademark of NRL. Computational resources for the COAMPSv4 simulations were supported in part by a grant of HPC time from the Department of Defense Major Shared Resource Centers, Wright Patterson Air Force Base, Ohio.

APPENDIX

Diagnosis of Surface Longwave Emissivity

The longwave emissivity ϵ of the land surface can be diagnosed from the model output, given downwelling and upwelling longwave radiation, L_d and L_u, respectively, and the surface (skin) temperature T_s. Upwelling longwave radiation is given by

$$L_u = L_e + (1 - \epsilon)L_d = \epsilon\sigma T_s^4 + (1 - \epsilon)L_d,$$

where $L_e = \epsilon\sigma T_s^4$ is the longwave emission of a graybody with temperature T_s. Solving for ϵ yields

$$\epsilon = \frac{L_u - L_d}{\sigma T_s^4 - L_d}.$$

REFERENCES

Berg, L. K., and S. Zhong, 2005: Sensitivity of MM5-simulated boundary layer characteristics to turbulence parameterizations. *J. Appl. Meteor.,* **44,** 1467–1483.

Blackadar, A. K., 1978: Modeling pollutant transfer during daytime convection. Preprints, *Fourth Symp. on Atmospheric Turbulence, Diffusion, and Air Quality,* Reno, NV, Amer. Meteor. Soc., 443–447.

Bonan, G. B., 2008: *Ecological Climatology: Concepts and Applications*. 2nd ed. Cambridge University Press, 568 pp.

Brehm, M., 1986: Experimental and numerical investigations of the slope wind layer and its role in the warming of valleys. Ph.D. thesis, Meteorologisches Institut, Universität München, Wiss. Mitt. 54, 150 pp.

Chen, C., and W. R. Cotton, 1983: A one-dimensional simulation of the stratocumulus-capped mixed layer. *Bound.-Layer Meteor.,* **25,** 289–321.

Chow, F. K., A. P. Weigel, R. L. Street, M. W. Rotach, and M. Xue, 2006: High-resolution large-eddy simulations of flow in a steep Alpine valley. Part I: Methodology, verification, and sensitivity experiments. *J. Appl. Meteor. Climatol.,* **45,** 63–86.

Cotton, W. R., and Coauthors, 2003: RAMS 2001: Current status and future directions. *Meteor. Atmos. Phys.,* **82,** 5–29.

Davies, T., M. J. P. Cullen, A. J. Malcolm, M. H. Mawson, A. Staniforth, A. A. White, and N. Wood, 2005: A new dynamical core for the Met Office's global and regional modelling of the atmosphere. *Quart. J. Roy. Meteor. Soc.,* **131,** 1759–1782.

De Wekker, S. F. J., D. G. Steyn, J. D. Fast, M. W. Rotach, and S. Zhong, 2005: The performance of RAMS in representing the convective boundary layer structure in a very steep valley. *Environ. Fluid Mech.,* **5,** 35–62.

Deardorff, J. W., 1980: Stratocumulus-capped mixed layers derived from a 3-dimensional model. *Bound.-Layer Meteor.,* **18,** 495–527.

Doms, G., and Coauthors, 2007: A description of the nonhydrostatic regional model LM: Part II: Physical parameterization. Tech. Rep., DWD, 146 pp.

Doran, J. C., J. D. Fast, and J. Horel, 2002: The VTMX 2000 campaign. *Bound.-Layer Meteor.,* **83,** 537–551.

Doyle, J. D., and Coauthors, 2000: An intercomparison of model-predicted wave breaking for the 11 January 1972 Boulder windstorm. *Mon. Wea. Rev.,* **128,** 901–914.

Dudhia, J., 1989: Numerical study of convection observed during the Winter Monsoon Experiment using a mesoscale two-dimensional model. *J. Atmos. Sci.,* **46,** 3077–3107.

——, 1993: A nonhydrostatic version of the Penn State/NCAR Mesoscale Model: Validation tests and simulation of an Atlantic cyclone and cold front. *Mon. Wea. Rev.,* **121,** 1493–1513.

Egger, J., 1990: Thermally forced flows: Theory. *Atmospheric Processes over Complex Terrain, Meteor. Monogr.,* No. 23, Amer. Meteor. Soc., 43–58.

Estoque, M. A., 1968: Vertical mixing due to penetrative convection. *J. Atmos. Sci.,* **25,** 1046–1051.

Grubisic, V., and Coauthors, 2008: The Terrain-induced Rotor Experiment: An overview of the field campaign and some highlights of special observations. *Bull. Amer. Meteor. Soc.,* **89,** 1513–1533.

Helfand, H. M., and J. C. Labraga, 1988: Design of a nonsingular level-2.5 second-order closure model for the prediction of atmospheric turbulence. *J. Atmos. Sci.,* **45,** 113–132.

Hodur, R. M., 1997: The Naval Research Laboratory's Coupled Ocean/Atmosphere Mesoscale Prediction System (COAMPS). *Mon. Wea. Rev.,* **125,** 1414–1430.

Holt, T. R., D. Niyogi, F. Chen, K. Manning, M. A. LeMone, and A. Quereshi, 2006: Effect of land–atmosphere interactions on the IHOP 24–25 May 2002 convection case. *Mon. Wea. Rev.,* **134,** 113–133.

Hong, S.-Y., Y. Noh, and J. Dudhia, 2006: A new vertical diffusion package with an explicit treatment of entrainment processes. *Mon. Wea. Rev.,* **134,** 2318–2341.

Hu, X.-M., J. W. Nielson-Gammon, and F. Zhang, 2010: Evaluation of three planetary boundary layer schemes in the WRF model. *J. Appl. Meteor. Climatol.,* **49,** 1831–1844.

Li, J. G., and B. W. Atkinson, 1999: Transition regimes in valley airflows. *Bound.-Layer Meteor.,* **91,** 385–411.

Lock, A. P., A. R. Brown, M. R. Bush, G. M. Martin, and R. N. B. Smith, 2000: A new boundary layer mixing scheme. Part I: Scheme description and single-column model tests. *Mon. Wea. Rev.,* **128,** 3187–3199.

McKee, T. B., and R. D. O'Neil, 1989: The role of valley geometry and energy budget in the formation of nocturnal valley winds. *J. Appl. Meteor.,* **28,** 445–456.

Mellor, G. L., and T. Yamada, 1982: Development of a turbulence closure model for geophysical fluid problems. *Rev. Geophys. Space Phys.,* **20,** 851–875.

Mlawer, E. J., S. J. Taubman, P. D. Brown, M. J. Iacono, and S. A. Clough, 1997: Radiative transfer for inhomogeneous atmospheres: RRTM, a validated correlated-k model for the longwave. *J. Geophys. Res.,* **102,** 16 663–16 682.

Prusa, J. M., P. K. Smolarkiewicz, and A. A. Wyszogrodzki, 2008: EULAG, a computational model for multiscale flows. *Comput. Fluids,* **37,** 1193–1207.

Rampanelli, G., D. Zardi, and R. Rotunno, 2004: Mechanisms of up-valley winds. *J. Atmos. Sci.,* **61,** 3097–3111.

Rotach, M. W., and Coauthors, 2004: Turbulence structure and exchange processes in an alpine valley: The Riviera project. *Bull. Amer. Meteor. Soc.,* **85,** 1367–1385.

——, M. Andretta, P. Calanca, A. P. Weigel, and A. Weiss, 2008: Boundary layer characteristics and turbulent exchange mechanisms in highly complex terrain. *Acta Geophys.,* **56,** 194–219.

Schmidli, J., and R. Rotunno, 2010: Mechanisms of along-valley winds and heat exchange over mountainous terrain. *J. Atmos. Sci.,* **67,** 3033–3047.

Schumann, U., 1991: Subgrid length-scales for large-eddy simulation of stratified turbulence. *Theor. Comput. Fluid Dyn.,* **2,** 269–290.

Sellers, P. J., and Coauthors, 1997: BOREAS in 1997: Experiment overview, scientific results, and future directions. *J. Geophys. Res.,* **102** (D24), 28 731–28 769.

Skamarock, W. C., and J. B. Klemp, 2008: A time-split nonhydrostatic atmospheric model for weather research and forecasting applications. *J. Comput. Phys.,* **227,** 3465–3485.

Steinacker, R., 1984: Area-height distribution of a valley and its relation to the valley wind. *Contrib. Atmos. Phys.,* **57,** 64–71.

Steppeler, J., G. Doms, U. Schättler, H. Bitzer, A. Gassmann, U. Damrath, and G. Gregoric, 2003: Meso-gamma scale forecasts using the nonhydrostatic model LM. *Meteor. Atmos. Phys.,* **82,** 75–96.

Sun, W.-Y., and C.-Z. Chang, 1986: Diffusion model for a convective layer. Part I: Numerical simulation of convective boundary layer. *J. Climate Appl. Meteor.,* **25,** 1445–1453.

Thompson, W. T., and S. D. Burk, 1991: An investigation of an Arctic front with a vertically nested mesoscale model. *Mon. Wea. Rev.,* **119,** 233–261.

Thunis, P., and Coauthors, 2003: An inter-comparison exercise of mesoscale flow models applied to an ideal case simulation. *Atmos. Environ.,* **37,** 363–382.

Troen, I., and L. Mahrt, 1986: A simple model of the atmospheric boundary layer – sensitivity to surface evaporation. *Bound.-Layer Meteor.,* **37,** 129–148.

Wagner, A., 1938: Theory and observations of periodic mountain winds. *Gerlands Beitr. Geophys.,* **52,** 408–449.

Weigel, A. P., F. K. Chow, M. W. Rotach, R. L. Street, and M. Xue, 2006: High-resolution large-eddy simulations of flow in a steep Alpine valley. Part II: Flow structure and heat budgets. *J. Appl. Meteor. Climatol.,* **45,** 87–107.

——, ——, and ——, 2007: On the nature of turbulent kinetic energy in a steep and narrow Alpine valley. *Bound.-Layer Meteor.,* **123,** 177–199, doi:10.1007/s10546-006-9142-9.

Whiteman, C. D., 1990: Observations of thermally developed wind systems in mountainous terrain. *Atmospheric Processes over Complex Terrain, Meteor. Monogr.,* No. 23, Amer. Meteor. Soc., 5–42.

——, 2000: *Mountain Meteorology: Fundamentals and Applications*. Oxford University Press, 355 pp.

Xue, M., K. K. Droegemeier, and V. Wong, 2000: The Advanced Regional Prediction System (ARPS)—A multi-scale nonhydrostatic atmospheric simulation and prediction model. Part I: Model dynamics and verification. *Meteor. Atmos. Phys.,* **75,** 161–193.

——, and Coauthors, 2001: The Advanced Regional Prediction System (ARPS)—A multi-scale nonhydrostatic atmospheric

simulation and prediction model. Part II: Model physics and applications. *Meteor. Atmos. Phys.,* **76,** 143–165.

Zängl, G., 2002: An improved method for computing horizontal diffusion in a sigma-coordinate model and its application to simulations over mountainous topography. *Mon. Wea. Rev.,* **130,** 1423–1432.

——, A. Gohm, and F. Obleitner, 2008: The impact of the PBL scheme and the vertical distribution of model layers on simulations of Alpine foehn. *Meteor. Atmos. Phys.,* **99,** 105–128.

Zhang, D., and R. A. Anthes, 1982: A high-resolution model of the planetary boundary layer—Sensitivity tests and comparison with SESAME-79 data. *J. Appl. Meteor.,* **21,** 1594–1609.

——, and W.-Z. Zheng, 2004: Diurnal cycles of surface winds and temperatures as simulated by five boundary layer parameterizations. *J. Appl. Meteor.,* **43,** 157–169.

Zhong, S. Y., and J. Fast, 2003: An evaluation of the MM5, RAMS, and Meso-Eta models at subkilometer resolution using VTMX field campaign data in the Salt Lake Valley. *Mon. Wea. Rev.,* **131,** 1301–1322.